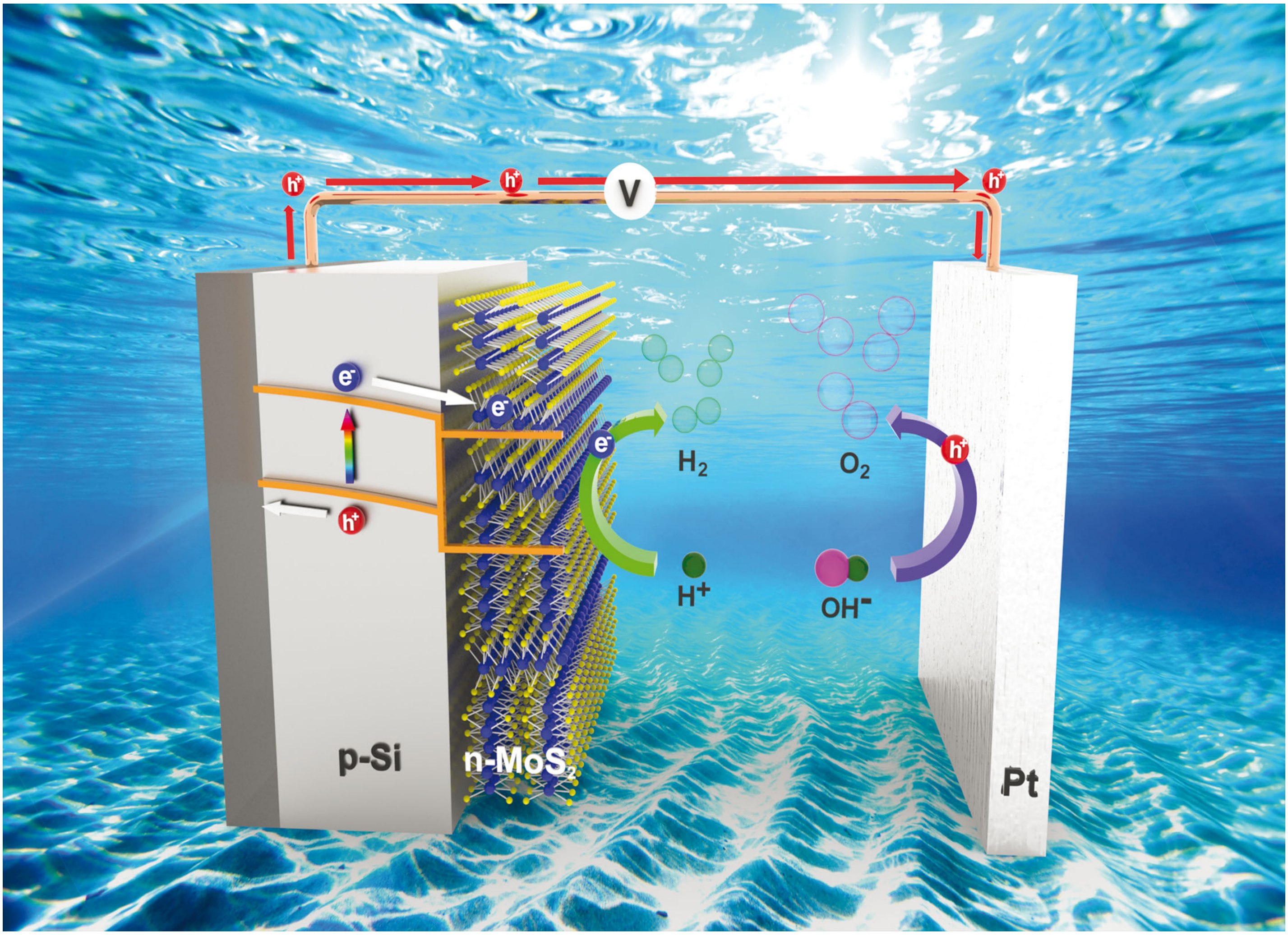


**Showcasing collaborative research from the laboratories of Prof. Soo Young Kim at Chung-Ang University, Korea, and Prof. Ho Won Jang at Seoul National University, Korea**

Wafer-scale transferable molybdenum disulfide thin-film catalysts for photoelectrochemical hydrogen production

The synthesis of $MoS_2$ thin films with c-domains of high hydrogen evolution reaction activity and the wafer-scale fabrication of n-$MoS_2$/p-Si heterojunction photocathodes using a simple transfer method are demonstrated.

## As featured in:


See Soo Young Kim, Ho Won Jang *et al.*, *Energy Environ. Sci.*, 2016, **9**, 2240.

Energy & Environmental Science

COMMUNICATION

View Article Online
View Journal | View Issue

Cite this: *Energy Environ. Sci.*, 2016, **9**, 2240

Received 15th January 2016, Accepted 21st March 2016

DOI: 10.1039/c6ee00144k

www.rsc.org/ees



# Wafer-scale transferable molybdenum disulfide thin-film catalysts for photoelectrochemical hydrogen production†

Ki Chang Kwon,‡[a] Seokhoon Choi,‡[a] Kootak Hong,[a] Cheon Woo Moon,[a] Young-Seok Shim,[a] Do Hong Kim,[a] Taemin Kim,[a] Woonbae Sohn,[a] Jong-Myeong Jeon,[a] Chul-Ho Lee,[b] Ki Tae Nam,[a] Seungwu Han,[a] Soo Young Kim*[c] and Ho Won Jang*[a]

**We demonstrate that wafer-scale, transferable, and transparent thin-film catalysts based on $MoS_2$, which consists of cheap and earth abundant elements, can provide a low onset potential of 1 mA cm$^{-2}$ at 0.17 V *versus* a reversible hydrogen electrode and the high photocurrent density of 24.6 mA cm$^{-2}$ at 0 V for a p-type Si photocathode. c-Domains with vertically stacked (100) planes in the transferable 2H-$MoS_2$ thin films, which are grown *via* a thermolysis method, act as active sites for the hydrogen evolution reaction, and photogenerated electrons are efficiently transported through the n-$MoS_2$/p-Si heterojunction.**

### Broader context

Hydrogen appears as a next-generation clean energy source to replace fossil fuels. One of the most promising ways to produce hydrogen is *via* photoelectrochemical (PEC) water splitting. However, the existing photoelectrodes such as Si with noble metal catalysts still suffer from low efficiency and poor stability and the extremely high cost of the noble metal catalysts limits the wide use of water splitting photoelectrodes. Therefore, a novel approach is necessary to make a breakthrough for highly efficient PEC water splitting. We have synthesized wafer-scale transferable molybdenum disulfide ($MoS_2$) thin-film catalysts by using the thermolysis method for the first time. Our results show that the $MoS_2$ thin-film catalysts not only reduce the overpotential at electrolyte/solid interfaces but also stabilize the surface of solids for efficient water splitting using p-type semiconductor photocathodes including Si, InP, GaAs, and GaP. Our approach could be applied to the synthesis of various 2-dimensional transition metal dichalcogenides (TMDs) and the catalytic performance of the materials would be further enhanced using substitutional doping, defect engineering, and n-TMD/p-TMD heterojunctions.

Photoelectrochemical (PEC) water splitting is a promising approach for the efficient and sustainable production of hydrogen as a fuel. In the pursuit of developing efficient and durable photoelectrodes, Si and III–V semiconductors have been extensively studied. These materials absorb wide ranges of the solar spectrum, including near-infrared (NIR) light, and the electrochemical potential for the hydrogen evolution reaction (HER) is within the band edges of the semiconductors.[1–3] p-Type Si is considered to be one of the most promising candidates for photocathode for HER because of its narrow band gap, earth abundance, and well-established production technology with relatively low costs. It also has the appropriate band energies to transport the photogenerated electrons to the hydrogen reduction potential ($H^+/H_2$). However, the surface of p-type Si has poor kinetics for absorbing the hydrogen ions ($H^+$). To achieve a higher solar-to-hydrogen efficiency, it requires a catalyst which can help the chemisorption or electrosorption of $H^+$.[4–6] In addition to this overpotential, Si is thermodynamically vulnerable to photoactive dissolution, or photocorrosion.[7] To reduce the overpotential, noble metals such as Pt, Rh, and Ir are widely used as HER catalysts in the form of nanoparticles. Unfortunately, these catalysts are relatively expensive and earth-deficient. Furthermore, the metal nanoparticles cannot prevent photocorrosion in p-type Si photocathodes. Although thick layers of noble metals can passivate the photocathodes, they drastically reduce light transmission through the metal layers, which lowers the photocurrent in the photocathodes, and the pinch-off

[a] *Department of Materials Science and Engineering, Research Institute of Advanced Materials, Seoul National University, Seoul 08826, Republic of Korea. E-mail: hwjang@snu.ac.kr*
[b] *KU-KIST Graduate School of Converging Science and Technology, Korea University, Seoul 136-701, Republic of Korea*
[c] *School of Chemical Engineering and Materials Science, Chung-Ang University, Seoul 156-756, Republic of Korea. E-mail: sooyoungkim@cau.ac.kr*

† Electronic supplementary information (ESI) available: Detailed experimental procedures and schematics (Fig. S1–S3), AFM images for various thicknesses (Fig. S4), SRPES analysis (Fig. S5), absorption spectra (Fig. S6), statistical PEC results (Fig. S7), cyclic tests (Fig. S8), chronoamperometry measurements (Fig. S9), electrochemical HER performance (Fig. S10), flat band diagram (Fig. S11), AFM images for surface morphology (Fig. S12), TEM analysis of Moiré fringes (Fig. S13), and additional HR-TEM analysis (Fig. S14). Video files are presented in the ESI for showing our PEC measurement system and for clarifying the different catalytic activities between bare p-Si and $MoS_2$/p-Si photocathodes. See DOI: 10.1039/c6ee00144k

‡ These authors contributed equally to this work.

 

phenomena of catalysts by which the desired catalytic reactions can be promoted cannot be exploited.[8] Therefore, a novel approach to simultaneously solve the overpotential and stability issues should be developed.

Two-dimensional transition-metal disulfides (2D TMDs) have attracted much attention as promising candidates to replace Pt, because TMD nanoparticles such as $MoS_2$ and $WS_2$ have inherently large surface-to-volume ratios and possess high densities of catalytically active edge sites for HER.[9,10] When TMDs are deposited on p-type semiconductors, such as p-type Si, the induced electrical fields between the TMDs and the p-type semiconductors would be very high because of the large difference in work function, which may increase the efficiency of transport of photogenerated electrons from the p-type semiconductors *via* the TMDs to the electrolyte/solid interfaces.

2D TMDs are usually obtained by exfoliation, solution-based syntheses, and chemical vapour deposition (CVD). Exfoliated and solution-processed TMDs nanoparticles have been reported to have many electrochemically active sites. However, as in noble metal particles, the fabrication of uniform, dense, and thin layers based on 2D TMD nanoparticles on the surface of p-type semiconductors is difficult.[11–14] Using CVD, uniform and ultrathin 2D TMD layers can be synthesized using powder precursors, such as $MoO_3$ and $MoCl_5$, on oxide substrates.[15–17] The surface of CVD-grown TMD layers contains electrochemically inactive basal planes.[18,19] The direct synthesis of ultrathin 2D TMD layers on p-type semiconductors is hindered by the lack of strong adhesion between the p-type semiconductors and 2D TMDs. For these reasons, a novel method that overcomes the limitations of nanoparticle-based coating and direct deposition is necessary to fabricate 2D TMD/p-type semiconductor heterojunctions.

Here, we demonstrate the wafer-scale fabrication of $MoS_2$/p-Si heterojunctions using a thin-film transfer method for high-performance PEC hydrogen production. Thickness-controlled $MoS_2$ layers were synthesized by the thermolysis of a solution precursor layer on $SiO_2$/Si substrates; these layers were transferred to p-Si wafers. The synthesized 2H-$MoS_2$ layers contain a-domains with layer-by-layer stacked (001) planes and c-domains with vertically stacked (100) planes. Since the electrochemically active c-domains act as HER catalytic sites and the n-$MoS_2$/p-Si heterojunction efficiently transports photogenerated electrons to the solid/electrolyte interface, the onset potential at a photocurrent of 1 mA $cm^{-2}$ is reduced by 0.445 V, which is one of the highest overpotential reduction values yet reported for HER catalysts without noble metals. The transferable $MoS_2$ thin-film catalyst reduces the overpotential of cathodes comprising p-InP, p-GaAs, and p-GaP, as well as p-Si.

The $MoS_2$ thin films used in this study were synthesized using a thermolysis system (see Fig. S1, ESI†). An ammonium tetramolybdate [$(NH_4)_2MoS_4$] precursor dissolved in ethylene glycol was spin-coated onto a $SiO_2$/Si substrate. Thermolysis at 500 °C under $N_2$ and $H_2$ flow converted the precursor to a $MoS_3$ layer. Subsequent heating to 900 °C in a reducing ambient atmosphere transformed the $MoS_3$ layer into a thin film of $MoS_2$.[20,21] Poly[methyl methacrylate] (PMMA) as a supporting polymer was spin-coated onto the synthesized $MoS_2$ thin films. The PMMA/$MoS_2$ thin films were separated from the $SiO_2$/Si substrates by immersion in a bath of HF and a buffered oxide etchant, and the separated films were transferred onto p-Si wafers. The PMMA supporting layer was removed using acetone, creating $MoS_2$/p-Si heterostructures. Backside contacts and epoxy passivation were established to allow PEC measurements. This experimental procedure is illustrated in Fig. 1(a). Fig. 1(b) shows a photographic image of a 6 cm × 6 cm $MoS_2$ thin film on a $SiO_2$/Si substrate. $MoS_2$ thin films could be grown on oxide substrates, such as $SiO_2$ and $Al_2O_3$, using the thermolysis method. The direct growth of $MoS_2$ thin films on p-Si wafers was difficult to achieve because of the poor adhesion between Si and $MoS_2$ (see Fig. S2, ESI†). Since the binding energy of S–O bonds exceeds that of S–Si bonds, $MoS_2$ could only be grown on oxides, not directly on Si.[22] Photographic images of a PMMA/$MoS_2$ membrane floating on deionized water and a 6 cm × 6 cm $MoS_2$ thin film on a 4 inch p-Si wafer are displayed in Fig. 1(c) and (d), respectively. To separate the $MoS_2$ thin films from $SiO_2$/Si substrates without introducing pinholes, controlling the etch rate of the $SiO_2$ layer was important (see Fig. S3, ESI†). Notably, the areas of the $MoS_2$ thin films are limited by the chamber size of the thermolysis system.

By changing the concentration of the precursor solution, the thickness of the $MoS_2$ thin films could be tailored to be ranged between 5 nm and 29 nm, which was determined by using AFM (see Fig. S4, ESI†). The transmittances of the $MoS_2$ thin films were measured by transferring the thin films onto glass substrates as shown in Fig. 2(a). The 5 nm-thick $MoS_2$ thin film is transparent with a high transmittance of ∼96% at 600 nm, while the 29 nm-thick $MoS_2$ thin film of a dark greenish-yellow color showed a transmittance of ∼22%, as displayed in Fig. 2(b). On the p-Si substrate, transmittance through the $MoS_2$ thin films can be increased because the difference of refractive index between p-Si substrate ($\eta$ = 4.298 at 500 nm) and $MoS_2$ thin films ($\eta$ = 5.675 at 500 nm) is smaller than that between the glass substrate ($\eta$ = 1.528 at 500 nm) and the $MoS_2$ thin films.[23–25] The chemical components and atomic ratios of the synthesized $MoS_2$ thin films were investigated using XPS. For $MoS_2$ thin films of different thicknesses, the atomic ratio of Mo to S was constant at 62% to 38%, consistent with previous reports (see Fig. S5, ESI†).[9,20] The Raman spectra of $MoS_2$ thin films with different thicknesses are shown in Fig. 2(c). As the film thickness increases, the gap between the peaks for in-plane ($E^1_{2g}$) and out-of-plane ($A_{1g}$) vibrational modes becomes wider. This originates from the stiffening of the out-of-plane mode and the relaxation of the in-plane mode, which decreases the peak intensity ratio of the $E^1_{2g}$ mode to the $A_{1g}$ mode (Fig. 2(d)).[26,27] From the absorption spectra (see Fig. S6, ESI†), it was found that the optical band edges of $MoS_2$ thin films shift to the longer wavelengths as the film thickness increases. To evaluate the optical band gap energies of the $MoS_2$ thin films more specifically, we used $(\alpha h\nu)^2$ *vs.* $h\nu$ plot, where $\alpha$ is the absorption coefficient of the film (see in more detail in Fig. S7, ESI†). The obtained band gap energies are plotted in Fig. 2(d). The change of band gap energy in our $MoS_2$ thin films evaluated by transmittance measurements is consistent with the previous report about band gap energies of $MoS_2$ films on Si substrates

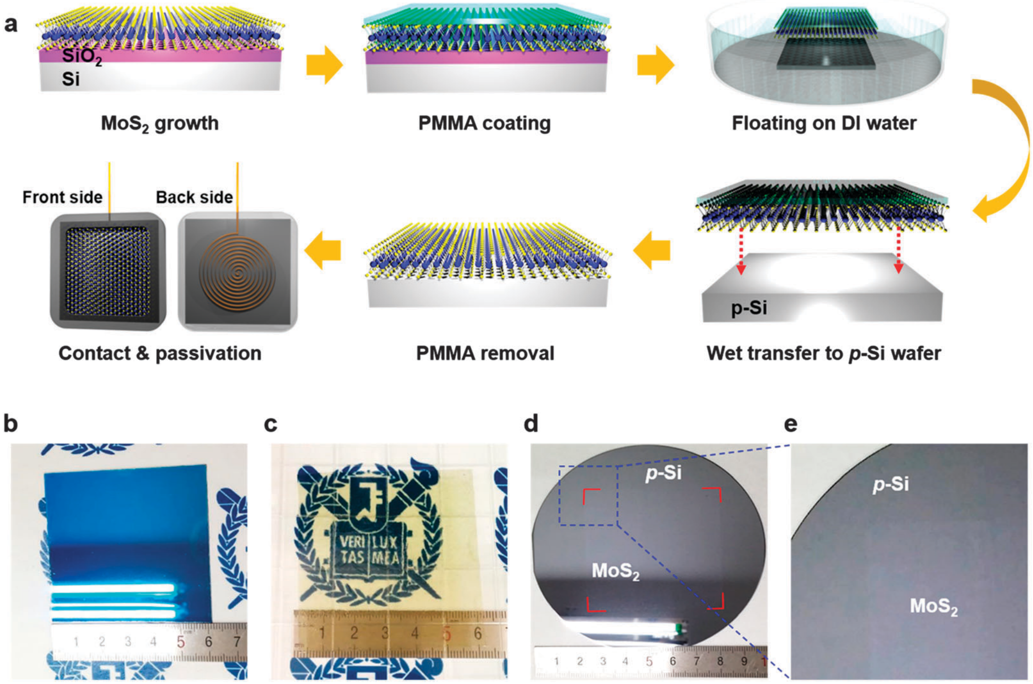


Fig. 1 Schematic of experimental procedure and photographic images of large-area synthesis of $MoS_2$ thin films. (a) Schematic of experimental procedures for the fabrication of $MoS_2$/p-Si photocathodes. Photographic images of (b) 100 mM $[(NH_4)_2MoS_4]$ spin-coated $SiO_2$ substrate, (c) synthesized $MoS_2$ floating in DI water bath, (d) transferred to 4 inch p-Si wafer, and (e) magnified image of (d).

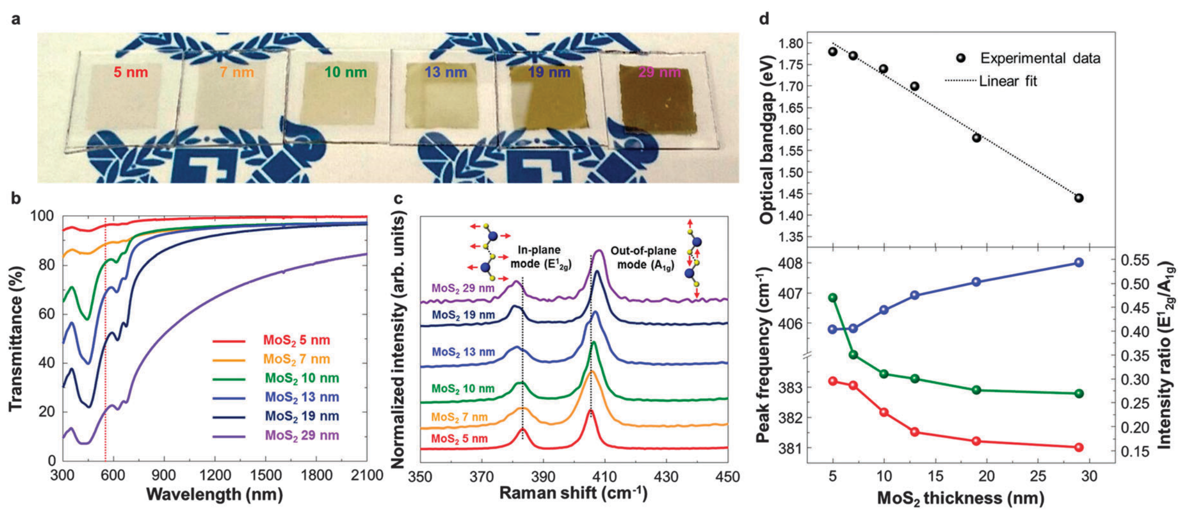


Fig. 2 Optical properties of the synthesized $MoS_2$ thin film with various thicknesses. (a) Photographic images of the transferred $MoS_2$ thin films on glass substrates. (b) The transmittance spectra of $MoS_2$ thin films. (c) The Raman spectra of synthesized $MoS_2$ films for each thickness. (d) The evaluated optical band gap of the synthesized $MoS_2$ thin film and Raman analysis of $MoS_2$ thin films with different thicknesses. The black dotted line indicates a linear fitting. The peak gap between $E^1_{2g}$ and $A_{1g}$ gradually increases as a function of $MoS_2$ film thickness. The intensity ratio of $E^1_{2g}$ to $A_{1g}$ is significantly decreased as the $MoS_2$ thickness is increased.

evaluated by reflectance measurements and optical properties of mechanically exfoliated $MoS_2$ layers.[28–30]

PEC measurements with the $MoS_2$/p-Si photocathodes were performed using a standard three-electrode cell with an electrolyte of 0.5 M sulfuric acid. Fig. 3(a) shows the photoelectrochemical current densities of the $MoS_2$/p-Si photocathodes plotted as a function of potential *vs.* reversible hydrogen electrode (RHE). The dark currents are shown as dashed lines. The bare p-Si photocathode exhibits a large onset potential of −0.28 V, defined as the potential at the photocurrent density of $-1$ mA $cm^{-2}$. Although p-Si is a widely used photocathode for solar water splitting, because it has a narrow band gap, high crystallinity, and low cost, a large potential must be applied to adsorb hydrogen ions on the surface of the material.[31] All $MoS_2$/p-Si



 

View Article Online




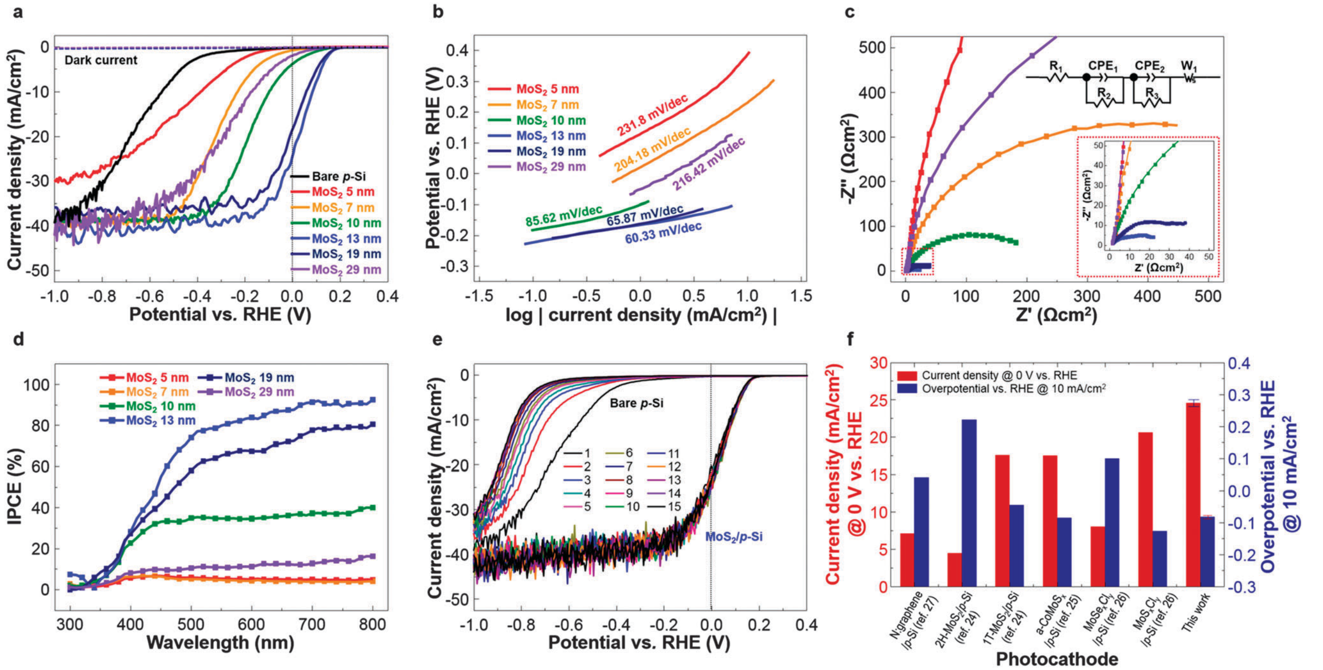


Fig. 3 Photoelectrochemical (PEC) and electrochemical impedance spectroscopic (EIS) analyses of the $MoS_2$/p-Si heterojunction photocathode system. (a) PEC performances shown as polarization *J–V* curves of $MoS_2$ films of different thicknesses. The 13 nm-thick $MoS_2$/p-Si photocathode shows 24.6 mA $cm^{-2}$ at 0 V and a significant potential value shift at 10 mA $cm^{-2}$ from −0.69 V for p-Si to 0.082 V. (b) Tafel slopes of $MoS_2$ layers plotted as log( *j*) against potential *vs.* RHE. The 13 nm-thick $MoS_2$/p-Si sample shows the lowest Tafel slope of 60.33 mV $dec^{-1}$. (c) EIS analysis of $MoS_2$/p-Si heterostructures. Inset graph magnifies the 0–50 Ω $cm^2$ results for better comprehension. (d) ICPE measurements of various thicknesses of $MoS_2$/p-Si photocathodes. (e) Cyclic test over 15 cycles to compare that stabilities of bare p-Si and $MoS_2$/p-Si photocathodes. (f) Comparison of PEC performance between our 13 nm-thick $MoS_2$/p-Si photocathode and previously reported state-of-the-art photocathodes using similar materials on planar p-Si.

photocathodes exhibit lower onset potentials than the p-Si photocathode. The onset potential gradually shifts toward the positive region until the thickness of the $MoS_2$ thin film reaches 13 nm. For the 13 nm-thick $MoS_2$/p-Si photocathode, the onset potential is 0.17 V and the photocurrent density at 0 V is −24.6 mA $cm^{-2}$. We emphasize that this value is even higher than the 17.6 mA $cm^{-2}$ photocurrent density measured at 0 V for a 1T-$MoS_2$/p-Si heterostructured photocathode, in which the $MoS_2$ film was directly synthesized on the p-Si substrate.[31] The curves in Fig. 3(a) are from the first scans for each $MoS_2$/p-Si heterojunction photocathode. The variation of current density in the negative potential regions originates from the use of a stirrer for detaching the hydrogen bubbles on the surface of $MoS_2$/p-Si photocathodes. Because of the transferred 13 nm-thick $MoS_2$ thin film, the potential at the photocurrent density of 10 mA $cm^{-2}$ is reduced from 0.69 V to −0.082 V for the fabricated photocathodes. When the $MoS_2$ thin films exceed 13 nm in thickness, the onset potential is shifted toward the negative region. We also calculated applied-bias photon-to-current efficiency (ABPE) from measurements, shown in Fig. 3(a). The maximum ABPE and open-circuit voltage are 0.86% and 0.46 V for the 13 nm-thick $MoS_2$/p-Si photocathodes, respectively. This result is comparable with the previously reported value for the 1T-$MoS_2$/p-Si photocathode (ABPE of ∼1%).[28] The Faradaic efficiency of the 13 nm-thick $MoS_2$/p-Si heterojunction photocathode was determined by collecting the evolved hydrogen gas. The results reveal that the $MoS_2$/p-Si photocathode gives almost 100% Faradaic yield during the PEC process, which is well-consistent with the previous reports (see Fig. S8, ESI†).[32,33]

To understand the catalytic activity of the transferred $MoS_2$ thin films, the polarization curves in Fig. 3(a) were converted to Tafel plots, in which the potentials are plotted as functions of the logarithm of current density. The linear portions of the curves are collected to evaluate the Tafel slopes in Fig. 3(b). Catalysts with high HER activities are known to have low Tafel slopes. The 13 nm-thick $MoS_2$/p-Si photocathode with the highest photocurrent at 0 V shows the lowest Tafel slope of 60.33 mV $dec^{-1}$. Interestingly, this value is very close to the Tafel slope of 2H-$MoS_2$ nanodots, which indicates that the transferred $MoS_2$ thin film works as an efficient HER catalyst for p-Si.[14] Water reduction for the evolution of hydrogen occurs *via* the accepted three-step mechanism, which includes the Volmer (Tafel slope of 120 mV $dec^{-1}$ in an acidic electrolyte), Heyrovsky (40 mV $dec^{-1}$), and Tafel (30 mV $dec^{-1}$) steps. The Tafel slope of 60.33 mV $dec^{-1}$ for the 13 nm-thick $MoS_2$/p-Si photocathode indicates that HER most likely occurs *via* the Volmer–Heyrovsky mechanism with this cathode structure.[14] 5 different samples for each $MoS_2$/p-Si photocathode showed a valuable difference in potential at 10 mA $cm^{-2}$, photocurrent densities at 0 V, and the Tafel slopes are summarized in Fig. S9 (see the ESI†).

Electrochemical impedance spectroscopy (EIS) measurements were conducted to understand the surface kinetics during HER in

Table 1 Comparison of charge-transfer resistance ($R_{ct}$) values

| Photocathode | $R_{ct,1}$ ($\Omega$ cm$^2$) contact/p-Si | $R_{ct,2}$ ($\Omega$ cm$^2$) p-Si/$MoS_2$ | $R_{ct,3}$ ($\Omega$ cm$^2$) $MoS_2$/EL[b] |
|---|---|---|---|
| p-Si | 1.17 | 4809.89[a] | — |
| 5 nm $MoS_2$/p-Si | 0.72 | 1066.58 | 2620.42 |
| 7 nm $MoS_2$/p-Si | 1.02 | 455.47 | 520.24 |
| 10 nm $MoS_2$/p-Si | 0.99 | 96.97 | 119.37 |
| 13 nm $MoS_2$/p-Si | 0.90 | 10.43 | 10.56 |
| 19 nm $MoS_2$/p-Si | 0.77 | 13.53 | 15.34 |
| 29 nm $MoS_2$/p-Si | 0.52 | 764.49 | 1063.03 |

[a] p-Si/electrolyte. [b] EL: electrolyte.

the acidic electrolyte. The impedance spectra, measured by applying a small voltage (−0.07 V) near the onset potential, reflect the HER activities of the photocatalysts. A high HER activity is reflected by a small semicircle in the Nyquist plots shown in Fig. 3(c). The smallest semicircle, demonstrated by the spectrum for the photocathode with a 13 nm-thick $MoS_2$ layer, represents the fastest electrode-to-electrolyte shuttling of electrons during HER. An equivalent circuit is composed of constant phase elements (CPE) and charge-transfer resistances ($R_{ct}$).[31] The variation of $R_{ct}$ at the $MoS_2$/electrolyte interfaces ($R_{ct,3}$) agrees with that of the photocurrents at 0 V in Fig. 3(a), as shown in Table 1. The $R_{ct}$ value for the 13 nm-thick $MoS_2$/p-Si photocathode is two orders of magnitude lower than that for the bare p-Si, indicating that the transferred 13 nm-thick $MoS_2$ thin film is critical for charge transfer at the solid/electrolyte interface. The incident-photon-to-current conversion efficiency (IPCE) spectra of the $MoS_2$/p-Si photocathodes, measured at −0.1 V *vs.* RHE, are displayed in Fig. 3(d). Throughout the tested spectrum, the photocathode with the 13 nm-thick $MoS_2$ layer shows the highest efficiency. Combined with the linear-sweep voltammetry curves, these results clearly show that the PEC properties of the $MoS_2$/p-Si photocathodes depend on the thickness of the $MoS_2$ thin film and that an optimum $MoS_2$ thin-film thickness exists.

The stability of the 13 nm-thick $MoS_2$/p-Si photocathodes was investigated to determine whether the transferred $MoS_2$ thin-film catalyst could act as a passivation layer. Fig. 3(e) shows the linear sweep voltammetry curves of bare p-Si and $MoS_2$/p-Si photocathodes for 15 cycles. The bare Si photocathode shows fast degradation, while the $MoS_2$/p-Si photocathode shows significant suppression of shifts toward more negative potentials throughout the measurement cycles. In order to investigate the thickness dependent stability of the fabricated electrodes, cyclic tests were performed for using 7 nm-thick, 13 nm-thick, and 29 nm-thick $MoS_2$/p-Si photocathodes. The stability of the electrodes was different from one another (see Fig. S10, ESI†). Especially, the lowest stability was found for the 29 nm-thick $MoS_2$/p-Si photocathode, where the top $MoS_2$ layers would have relatively weak van der Waals force compared to the bottom $MoS_2$ films which are located at the heterointerface with the p-Si. The stability enhancement by the transferred $MoS_2$ thin film was confirmed by chronoamperometry measurements (see Fig. S11, ESI†). From the normalized chronoamperometric curves of Pt decorated bare p-Si and Pt decorated $MoS_2$/p-Si photocathodes, measured at 0 V *vs.* RHE, it is observed that the current density of the Pt decorated bare p-Si photocathode decreases rapidly during the measurement and retains only 0.1% of the original current density after 9.6 hours. As aforementioned in the Introduction, the photocorrosion of the p-Si photocathode cannot be prevented using Pt nanoparticles. Meanwhile, the Pt decorated $MoS_2$/p-Si photocathode maintains the initial current density even after 50 hours, demonstrating the behavior of the transferred $MoS_2$ thin film as a passivation layer that prevents the p-Si photocathode from experiencing severe photocorrosion.[31] To clarify the passivation effect of the $MoS_2$ thin film, we have measured the stability of the photocathode using a fritted Pt counter electrode, which is free from dissolving in the strong acid electrolyte (0.5 M $H_2SO_4$, pH = 1.1) (see Fig. S12, ESI†). For the $MoS_2$/p-Si photocathode, the current density was stable after 50 hours without notable degradation, indicating that the transferred $MoS_2$ thin film acts as not only a catalyst for hydrogen production but also an excellent passivation layer. We have also investigated the electrochemical HER performance of $MoS_2$ thin films with various thicknesses on the Au substrate without iR-correction (see Fig. S13, ESI†). The HER performance of our synthesized $MoS_2$ thin films is comparable to that of the previously reported $MoS_2$ catalysts.[9–11,13] The slightly lower overpotentials and Tafel slopes of the $MoS_2$/p-Si photocathodes compared with those of the $MoS_2$ thin films indicate that the downward band bending in p-Si promotes HER at the solid/electrolyte interface.

In order to compare the PEC performance of the 13 nm-thick $MoS_2$/p-Si photocathode with that of previously reported state-of-the-art photocathodes with similar material systems, photocurrent densities at 0 V *vs.* RHE and overpotentials *vs.* RHE at 10 mA cm$^{-2}$ for our $MoS_2$/p-Si photocathode and other photocathodes based on TMD material (or graphene)/p-Si heterostructures without noble metal catalysts have been plotted in Fig. 3(f).[31,34–37] The overpotential at 10 mA cm$^{-2}$ of our photocathode is lower than those of other photocathodes including the 1T-$MoS_2$/p-Si photocathode and close to that of chlorine-doped $MoS_x$ ($MoS_xCl_y$)/p-Si photocathodes.[31,35] For the photocurrent densities at 0 V *vs.* RHE, it is clear that our photocathode shows the highest value among the material systems. The details about the material systems and numerical values are summarized in the ESI,† Table S1.

Because the transferred $MoS_2$ thin films are semitransparent, most incident light is absorbed in the underlying p-Si substrate of the $MoS_2$/p-Si heterostructured photocathodes. Thus, the photogenerated electrons in p-Si should be efficiently transported to the $MoS_2$/electrolyte interface for HER. Band-bending in the $MoS_2$/p-Si heterostructures was investigated using ultraviolet photoemission spectroscopy (UPS) and XPS. The secondary electron emission (SEE) spectra of the bare p-Si, 13 nm-thick $MoS_2$/p-Si, and reference Au foil electrodes are displayed in Fig. 4(a). Compared with the work function of the Au reference (5.1 eV), the work functions of the samples can be estimated from the SEE cutoffs as 4.7 eV and 4.5 eV for p-Si and $MoS_2$/p-Si, respectively. According to the XPS valence-band spectra displayed in Fig. 4(b), the energy difference between the Fermi level and the valence band maximum ($E_F - E_V$) for bare p-Si is 0.5 eV, indicating

 

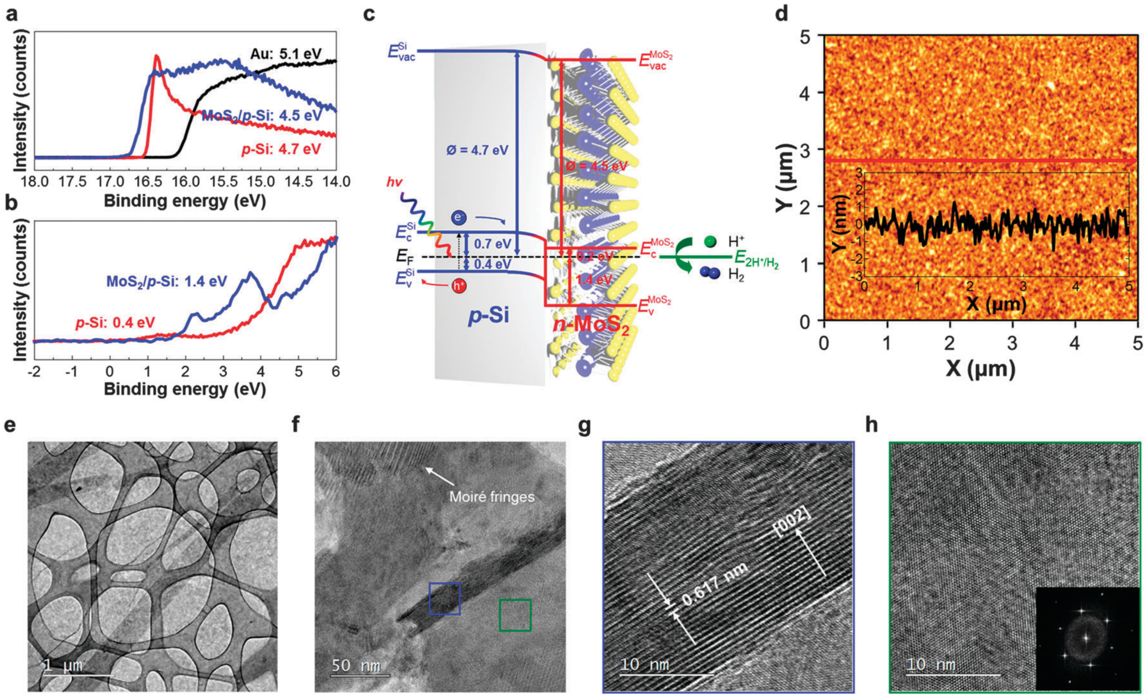


Fig. 4 Characterization of $MoS_2$ thin film (13 nm) grown by using the solution precursor-based thermolysis method. (a) UPS spectra of p-Si, 13 nm-thick $MoS_2$/p-Si, and reference Au foil. (b) XPS spectra of p-Si, 13 nm-thick $MoS_2$/p-Si, and reference Au foil. (c) Schematic of energy band diagram of the $MoS_2$/p-Si heterojunction photocathode. (d) AFM image of the $MoS_2$ thin film on the $SiO_2$/Si substrate. (e) and (f) TEM images of the synthesized $MoS_2$ thin film with different magnifications. The high-resolution TEM images of (g) c-domains with vertically stacked (001) planes and (h) a-domains with horizontally stacked (001) planes. The SAED pattern of synthesized $MoS_2$ thin film is displayed in the inset of (h).

a downward band bending of ∼0.3 eV. The $E_F - E_V$ for $MoS_2$/p-Si is 1.4 eV. Because the photoelectrons escape depth of ∼5 nm is less than the thickness of the $MoS_2$ layer, and because the $MoS_2$ layer with an optical bandgap energy of 1.6 eV (see Fig. S6, ESI†) has negligible surface band bending, the Fermi level of $MoS_2$ is determined to be 0.2 eV below the conduction-band maximum ($E_C$). This reveals that the transferred $MoS_2$ thin film is an n-type semiconductor.[37] Based on these results, the energy band diagram for the n-$MoS_2$/p-Si heterojunction is illustrated in Fig. 4(c). Flat band and band bending diagrams for the n-$MoS_2$/p-Si heterojunction are displayed in Fig. S14 (see the ESI†). The Fermi level should be equalized when both n- and p-type materials make the heterojunction. By assuming that the band bending in the p-Si for the $MoS_2$/p-Si heterojunction is similar to that for the bare p-Si, the n-$MoS_2$/p-Si heterojunction is found to form a type-II junction as described in Fig. 4(c). The band diagram clearly shows that the transport of photogenerated electrons from p-Si to $MoS_2$ is energetically favorable. Interestingly, the $E_C$ level of the $MoS_2$ layer is equal to the $H^+/H_2$ reduction potential (4.5 eV), suggesting that electrons can be effectively transferred to the electrolyte without an electronic potential barrier.[38,39]

The overall quantum efficiency of the n-$MoS_2$/p-Si photocathode largely depends on the overpotential for HER at the n-$MoS_2$/electrolyte interface. The surface morphology of the transferred $MoS_2$ thin films was examined by AFM. All synthesized $MoS_2$ thin films were nano-granular (see Fig. S15, ESI†). For the 13 nm-thick $MoS_2$ thin film, the root-mean-square (RMS) roughness was ∼1.5 nm with a peak-to-valley depth of ∼2 nm, as seen in Fig. 4(d). The serrated surface of the 2H-$MoS_2$ thin film provides a larger surface area than the atomically flat surface of a single-crystalline $MoS_2$ monolayer. The relatively high RMS roughness originates from the coexistence of a-domains and c-domains which have different growth rates and domain boundaries between them. Furthermore, the partially rotated $MoS_2$ basal planes, Moiré fringes, roughen the surface of the transferred $MoS_2$ thin film as observed in Fig. S16 (ESI†). The microstructure of the $MoS_2$ thin films was studied using transmission electron microscopy (TEM). The low-magnification TEM image in Fig. 4(e) shows a pinhole-free 13 nm-thick $MoS_2$ thin film with some wrinkles on a meshed Cu grid. High-resolution TEM images are shown in Fig. 4(f)–(h). Clearly, the films mainly contain a-domains with the preferred out-of-plane (001) orientation of the 2H-$MoS_2$ phase and c-domains with the preferred in-plane (001) orientation of the 2H-$MoS_2$ phase. From some a-domain regions, Moiré fringes from in-plane rotation between two basal planes were observed (see Fig. S16, ESI†).[40] Crystallographically, the surfaces of the a-domains are free of dangling bonds, while some dangling bonds exist at the surfaces of c-domains. Because the dangling bonds are electrochemically active sites for HER, the $MoS_2$ film with c-domains should act as an efficient HER catalyst, as observed in Fig. 3.[16] The presence of c-domains with vertically stacked (001) planes of the 2H-$MoS_2$ phase is the main advantage of our solution-based thermolytic method compared to CVD methods, where a-domains

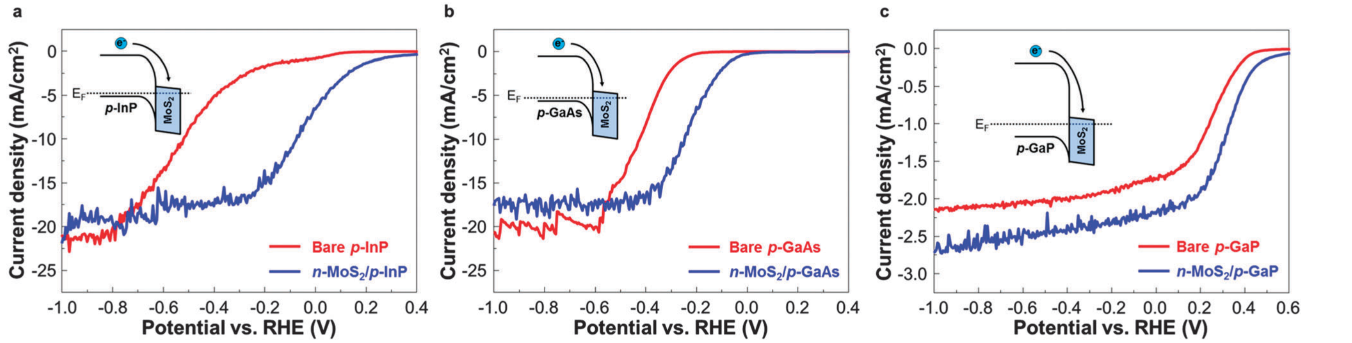


Fig. 5 Polarization curves of 13 nm $MoS_2$/p-type semiconductor heterojunction photocathodes. The polarization $J$–$V$ curves of (a) 13 nm-thick n-$MoS_2$/p-InP photocathode, (b) 13 nm-thick n-$MoS_2$/p-GaAs photocathode, and (c) 13 nm-thick n-$MoS_2$/p-GaP photocathode. Insets show the energy band diagram of each heterojunction.



of the 2H-$MoS_2$ phase are preferentially synthesized on foreign substrates. During the thermolysis, the growth of randomly oriented nuclei in the precursor layer resulted in the formation of both c-domains and a-domains. We found that thicker $MoS_2$ thin films had higher degrees of crystallinity and larger c-domains (see Fig. S17, ESI†), which implied that the thicker $MoS_2$ thin films could have higher HER activity than the thinner films, as observed in Fig. 3(a). Although the 29 nm-thick $MoS_2$ thin film would have a high HER activity, the increased attenuation of light in the $MoS_2$ film would reduce the light absorption in the underlying p-Si substrate, where the photogenerated electrons are located in energy levels higher than those in the $MoS_2$ film. As a result, the 29 nm-thick n-$MoS_2$/p-Si photocathode shows a higher overpotential than the 13 nm-thick n-$MoS_2$/p-Si photocathode.

The novel aspect of the n-$MoS_2$ thin-film catalysts developed here is the transferability onto other substrates. To demonstrate the versatility of the thin-film catalysts, we employed various p-type III–V semiconductors as photoelectrodes. Using the same procedure for the fabrication of the n-$MoS_2$/p-Si photocathodes, 13 nm-thick $MoS_2$ thin films were transferred to p-InP, p-GaAs, and p-GaP substrates. The PEC properties of the fabricated heterojunction photocathodes are shown in Fig. 5. Under AM 1.5 G solar illumination, the bare p-type semiconductors show varied saturation photocurrents and onset potentials because of the different band gap energies (1.3 eV for InP, 1.4 for GaAs, and 2.3 eV for GaP). The onset potentials, which depend on the $E_C$ levels and the overpotentials at the solid/liquid interfaces, also differ for the bare photocathodes. When the $MoS_2$ thin films are transferred to the p-InP, p-GaAs, and p-GaP substrates, the onset potentials are shifted toward the anodic direction without notable losses in the saturation photocurrents, indicating that the transferred $MoS_2$ thin films work as efficient catalysts for HER on the III–V semiconductor substrates.[41–43] Among the n-$MoS_2$/p-type semiconductor photocathodes, the n-$MoS_2$/p-Si heterojunction shows the best HER performance. It should be noted that Si is the cheapest and most earth-abundant material among the semiconductors. Because the band bending in the n-$MoS_2$/p-III–V heterojunctions is large, as illustrated in the insets of Fig. 5, further reduction of the overpotential may be achieved by optimizing the back contacts and surface treatments for the III–V semiconductors. We believe that the transferred n-$MoS_2$ thin-film HER catalysts can be applied not only to other semiconductor photocathodes, but also to oxide-based photocathodes such as $Cu_2O$ and $SnO_x$.[44,45]

## Conclusions

We have successfully demonstrated the synthesis of $MoS_2$ thin films with high HER activities via solution-based thermolysis, as well as the wafer-scale fabrication of n-$MoS_2$/p-Si heterojunction photocathodes using a simple transfer method. The heterojunction photocathodes provide high photocurrent density (24.6 mA $cm^{-2}$ at 0 V *vs.* RHE), large shifts in overpotential (0.79 V at 10 mA $cm^{-2}$), and long-term stability (over 10 000 s). We expanded our work to verify the efficient HER catalytic activity of n-$MoS_2$ thin films transferred to other p-type semiconductors (p-InP, p-GaAs, and p-GaP). Our approach can be applied to various 2D TMDs, in which the HER activity of the TMDs can be enhanced through substitutional doping and defect engineering,[46] as well as n-TMD/p-TMD heterojunctions, in which the high electric fields in the atomically thin TMD p–n junctions can further enhance the efficiency of HER.[47] Although this study focused on the enhanced catalytic activity and stability of transferable $MoS_2$ thin films, wafer-scale TMD thin films could be useful in various electronic and optoelectronic devices, even those using curved or flexible substrates.[19]

## Author contributions

H. W. Jang and S. Y. Kim conceived and supervised the project. K. C. Kwon and S. Choi synthesized the $MoS_2$ thin films, fabricated the devices, and analyzed the results. K. Hong conducted the AFM measurements. C. W. Moon and Y.-S. Shim conducted EIS and IPCE measurements. W. Sohn and J.-M. Jeon obtained the TEM images. D. H. Kim and T. Kim conducted the SRPES measurements. C.-H. Lee, K. T. Nam and S. Han gave an idea on the formation of n-$MoS_2$/p-Si heterojunction. The manuscript was mainly written and revised by K. C. Kwon,

 

S. Choi, S. Y. Kim, and H. W. Jang. All authors discussed the results and commented on the manuscript.

## Acknowledgements

This work was supported by the Samsung Research Funding Center of Samsung Electronics. Ki Chang Kwon acknowledges the Global PhD Fellowship Program through the National Research Foundation of Korea funded by the Ministry of Education.

## Notes and references


1 A. J. Nozik, *Appl. Phys. Lett.*, 1976, **29**, 150–153.
2 A. J. Nozik, *Appl. Phys. Lett.*, 1977, **30**, 567–569.
3 L. Fornarini, A. J. Nozik and B. A. Parkinson, *J. Phys. Chem.*, 1984, **88**, 3238–3243.
4 E. L. Warren, S. W. Boettcher, J. R. McKone and N. S. Lewis, *SPIE-Int. Soc. Opt. Eng.*, 2010, **7770**, 77701.
5 N. C. Strandwitz, D. B. Turner-Evans, A. C. Tamboli, C. T. Chen, H. A. Atwater and N. S. Lewis, *Adv. Energy Mater.*, 2012, **2**, 1109–1116.
6 D. M. Andoshe, J.-M. Jeon, S. Y. Kim and H. W. Jang, *Electron. Mater. Lett.*, 2015, **11**, 323–335.
7 K. Osseo-Asare, D. Wei and K. K. Mishra, *J. Electrochem. Soc.*, 1996, **143**, 749–751.
8 M. G. Walter, E. L. Warren, J. R. McKone, S. W. Boettcher, Q. Mi, E. A. Santori and N. S. Lewis, *Chem. Rev.*, 2010, **110**, 6446–6473.
9 D. Voiry, M. Salehi, R. Silva, T. Fujita, M. Chen, T. Asefa, V. B. Shenoy, G. Eda and M. Chhowalla, *Nano Lett.*, 2013, **13**, 6222–6227.
10 L. Cheng, W. Huang, Q. Gong, C. Liu, Z. Liu, Y. Li and H. Dai, *Angew. Chem., Int. Ed.*, 2014, **53**, 7860–7863.
11 D. Voiry, H. Yamaguchi, J. Li, R. Silva, D. C. B. Alves, T. Fujita, M. Chen, T. Fujita, M. Chen, T. Asefa, V. B. Shenoy, G. Eda and M. Chhowalla, *Nat. Mater.*, 2013, **12**, 850–855.
12 L. Zhang, C. Liu, A. B. Wong, J. Resasco and P. Yang, *Nano Res.*, 2015, **8**, 281–287.
13 A. B. Laursen, S. Kegnæs, S. Dahl and I. Chorkendorff, *Energy Environ. Sci.*, 2012, **5**, 5577–5591.
14 J. Benson, M. Li, S. Wang, P. Wang and P. Papakonstantinou, *ACS Appl. Mater. Interfaces*, 2015, **7**, 14113–14122.
15 Y.-H. Lee, X.-Q. Zhang, W. Zhang, M.-T. Chang, C.-T. Lin, K.-D. Chang, Y.-C. Yu, J. T.-W. Wang, C.-S. Chang, L.-J. Li and T.-W. Lin, *Adv. Mater.*, 2012, **24**, 2320–2325.
16 X. Wang, H. Feng, Y. Wu and L. Jiao, *J. Am. Chem. Soc.*, 2013, **135**, 5304–5307.
17 Y. Yu, C. Li, Y. Liu, L. Su, Y. Zhang and L. Cao, *Sci. Rep.*, 2013, **3**, 1866.
18 T. F. Jaramillo, K. P. Jørgensen, J. Bonde, J. H. Nielsen, S. Horch and I. Chorkendorff, *Science*, 2007, **317**, 100–102.
19 Y. Yang, H. Fei, G. Ruan, C. Xiang and J. M. Tour, *Adv. Mater.*, 2014, **26**, 8163–8168.
20 K. C. Kwon, C. Kim, Q. V. Le, S. Gim, J. M. Jeon, J. Y. Ham, J.-L. Lee, H. W. Jang and S. Y. Kim, *ACS Nano*, 2015, **9**, 4146–4155.
21 K.-K. Liu, W. Zhang, Y.-H. Lee, Y.-C. Lin, M.-T. Chang, C.-Y. Su, C.-S. Chang, H. Li, Y. Shi, H. Zhang, C.-S. Lai and L.-J. Li, *Nano Lett.*, 2012, **12**, 1538–1544.
22 X. Jia, L. Yu, J. Liu, Q. Xu, M. Sickert, L. Chen and M. Lautens, *Green Chem.*, 2014, **16**, 3444–3449.
23 D. E. Aspnes and J. B. Theeten, *J. Electrochem. Soc.*, 1980, **127**, 1359–1365.
24 M. Rubin, *Sol. Energy Mater.*, 1985, **12**, 275–288.
25 H. Zhang, Y. Ma, Y. Wan, X. Rong, Z. Xie, W. Wang and L. Dai, *Sci. Rep.*, 2015, **5**, 8440.
26 H. Li, Q. Zhang, C. C. R. Yap, B. K. Tay, T. H. T. Edwin, A. Olivier and D. Baillargeat, *Adv. Funct. Mater.*, 2012, **22**, 1385–1395.
27 A. Berkdemir, H. R. Gutiérrez, A. R. B. Méndez, N. P. López, A. L. Elías, C.-I. Chia, B. Wang, V. H. Crespi, F. López-Urías, J.-C. Charlier, H. Terrones and M. Terrones, *Sci. Rep.*, 2013, **3**, 1755.
28 C. Yim, M. O'Brien, N. McEvoy, S. Winters, I. Mirza, J. G. Lunney and G. S. Duesberg, *Appl. Phys. Lett.*, 2014, **104**, 103114.
29 K. F. Mak, C. Lee, J. Hone, J. Shan and T. F. Heinz, *Phys. Rev. Lett.*, 2010, **105**, 136805.
30 H. S. Lee, S.-W. Min, Y.-G. Chang, M. K. Park, T. Nam, H. Kim, J. H. Kim, S. Ryu and S. Im, *Nano Lett.*, 2012, **12**, 3695–3700.
31 Q. Ding, F. Meng, C. R. English, M. Cabán-Acevedo, M. J. Shearer, D. Liang, A. S. Daniel, R. J. Hamers and S. Jin, *J. Am. Chem. Soc.*, 2014, **136**, 8504–8507.
32 X. Guo, G. Cao, F. Ding, X. Li, S. Zhen, Y. Xue, Y. Yan, T. Liu and K. Sun, *J. Mater. Chem. A*, 2015, **3**, 5041–5046.
33 J. Huang, D. Hou, Y. Zhou, W. Zhou, G. Li, Z. Tang, L. Li and S. Chen, *J. Mater. Chem. A*, 2015, **3**, 22886–22891.
34 Y. Chen, P. D. Tran, P. Boix, Y. Ren, S. Y. Chiam, Z. Li, K. Fu, L. H. Wong and J. Barber, *ACS Nano*, 2015, **9**, 3829–3836.
35 U. Sim, T.-Y. Yang, J. Moon, J. An, J. Hwang, J.-H. Seo, J. Lee, K. Y. Kim, J. Lee, S. Han, B. H. Hong and K. T. Nam, *Energy Environ. Sci.*, 2013, **6**, 3658–3664.
36 Q. Ding, J. Zhai, M. Cabán-Acevedo, M. J. Shearer, L. Li, H.-C. Chang, M.-L. Tsai, D. Ma, X. Zhang, R. J. Hamers, J.-H. He and S. Jin, *Adv. Mater.*, 2015, **27**, 6511–6518.
37 M.-L. Tsai, S.-H. Su, J.-K. Chang, D.-S. Tsai, C.-H. Chen, C.-I. Wu, L.-J. Li, L.-J. Chen and J.-H. He, *ACS Nano*, 2014, **8**, 8317–8322.
38 L. Ji, M. D. McDaniel, S. Wang, A. B. Posadas, X. Li, H. Huang, J. C. Lee, A. A. Demkov, A. J. Bard, J. G. Ekerdt and E. T. Yu, *Nat. Nanotechnol.*, 2015, **10**, 84–90.
39 K. F. Mak, C. Lee, J. Hone, J. Shan and T. F. Heinz, *Phys. Rev. Lett.*, 2010, **105**, 136805.
40 J. Reyes-Gasga, S. Tehuacanero and M. J. Yacamán, *Microsc. Res. Tech.*, 1998, **40**, 2–9.
41 A. J. Ritenour, J. W. Boucher, R. DeLancey, A. L. Greenaway, S. Aloni and S. W. Boettcher, *Energy Environ. Sci.*, 2015, **8**, 278–285.

42 M. Malizia, B. Seger, I. Chorkendorff and P. C. K. Vesborg, *J. Mater. Chem. A*, 2014, **2**, 6847–6853.
43 L. Gao, Y. Cui, J. Wang, A. Cavalli, A. Standing, T. T. T. Vu, M. A. Verheijen, J. E. M. Haverkort, E. P. A. M. Bakkers and P. H. L. Notten, *Nano Lett.*, 2014, **14**, 3715–3719.
44 C. G. Morales-Guio, L. Liardet, M. T. Mayer, S. D. Tilley, M. Grätzel and X. Hu, *Angew. Chem., Int. Ed.*, 2015, **54**, 664–667.
45 Y. Huang, Y.-E. Miao, J. Fu, S. Mo, C. Wei and T. Liu, *J. Mater. Chem. A*, 2015, **3**, 16263–16271.
46 L. Yang, K. Majumdar, H. Liu, Y. Du, H. Wu, M. Hatzistergos, P. Y. Hung, R. Tieckelmann, W. Tsai, C. Hobbs and P. D. Ye, *Nano Lett.*, 2014, **14**, 6275–6280.
47 C.-H. Lee, G.-H. Lee, A. M. van der Zande, W. Chen, Y. Li, M. Han, X. Cui, G. Arefe, C. Nuckolls, T. F. Heinz, J. Guo, J. Hone and P. Kim, *Nat. Nanotechnol.*, 2014, **9**, 676–681.